# Assessment of organ and effective dose when using region-of-interest attenuators in cone-beam CT and interventional fluoroscopy

Zhenyu Xiong
Sarath Vijayan
Stephen Rudin
Daniel R. Bednarek

# Assessment of organ and effective dose when using region-of-interest attenuators in cone-beam CT and interventional fluoroscopy

**Zhenyu Xiong,**[a,b,*] **Sarath Vijayan,**[a,b] **Stephen Rudin,**[a,b,c] **and Daniel R. Bednarek**[a,b,c]
[a]University at Buffalo, Medical Physics Program, Buffalo, New York, United States
[b]University at Buffalo, Toshiba Stroke and Vascular Research Center, Buffalo, New York, United States
[c]University at Buffalo, Department of Radiology, Buffalo, New York, United States

**Abstract.** In some medical-imaging procedures using cone-beam CT (CBCT) and fluoroscopy, only the center of the field of view (FOV) may be needed to be visualized with optimal image quality. To reduce the dose to the patient while maintaining visualization of the entire FOV, a Cu attenuator with a circular aperture for the region of interest (ROI) is used. The potential organ and effective dose reductions of ROI imaging when applied to CBCT and interventional fluoroscopic procedures were determined using EGSnrc Monte Carlo code. The Monte Carlo model was first validated by comparing the surface dose distribution in a solid-water block phantom with measurement by Gafchromic film. The dependence of dose reduction on the ROI attenuator thickness, the opening size of the ROI, the axial beam position, and the location of the different organs for both neuro and thoracic imaging was evaluated. The results showed a reduction in most organ doses of 45% to 70% and in effective dose of 46% to 66% compared to the dose in a CBCT scan and in an interventional procedure without the ROI attenuator. This work provides evidence of a substantial reduction of organ and effective doses when using an ROI attenuator during CBCT and fluoroscopic procedures. © *2017 Society of Photo-Optical Instrumentation Engineers (SPIE)* [DOI: [10.1117/1.JMI.4.3.031210](10.1117/1.JMI.4.3.031210)]

## 1 Introduction

Fluoroscopically guided interventions (FGI) include many different procedures, such as percutaneous coronary interventions, electrophysiology studies, endovascular aneurysm repair, embolizations, thrombolytic therapies, angioplasties, and stent placements. Cone-beam CT (CBCT) performed with the C-arm fluoroscopic system offers three-dimensional (3-D) information on patient anatomy that can be used as an adjunct to conventional digital subtraction angiography (DSA) and fluoroscopy during interventional procedures. These procedures often involve high radiation dose to the patient's skin and internal organs. The International Commission on Radiological Protection (ICRP) has recently published a report on the effects of radiation, in which it recognizes that some organs and tissue may be more sensitive to ionizing radiation than previously thought.[1] For example, the dose threshold for the formation of lens opacities was reduced from 5 Gy[2] in the case of acute irradiation of the eye lens to 0.5 Gy,[1] and an absorbed-dose threshold to the brain of 0.5 Gy was determined as likely to produce cerebrovascular disease.[1]

Not all FGI procedures require the highest image quality throughout the field of view (FOV) but only within a region of interest (ROI) where the interventional activity is occurring. Lower quality may be acceptable in the periphery of the image, which is primarily used for reference. We have previously developed an ROI attenuator method to reduce dose in regions of low interest and preserve high image quality in the ROI.[3,4] ROI

imaging techniques were introduced because of increasing concern about patient radiation exposure during fluoroscopic procedures.[3] This work focused on ROI fluoroscopy to reduce the dose administered to a patient during an interventional endovascular procedure under x-ray guidance. To reduce the dose outside the ROI, an x-ray attenuating filter with a central opening is placed in the beam. During x-ray imaging, the attenuator effectively lowers the dose in the peripheral region while allowing high quality imaging of the ROI. This work was extended to real-time equalization of ROI fluoroscopic images using binary masks,[5] and a thorough evaluation of this work in a clinical setting has been performed.[6]

Also, C-arm CBCT provides 3-D visualization of the vasculature and is frequently used as part of neurovascular diagnostic and interventional procedures, as it facilitates diagnosis and planning the treatment of intracranial aneurysms and other pathologies.[7–9] Compared with conventional two-dimensional DSA, 3-D CBCT provides more detailed information for the assessment of cerebral aneurysms and allows a more exact depiction of anatomic details that are beneficial for interventional surgery. A number of papers have described the use of ROI attenuators in CBCT.[10–14]

Although measurements of dose reduction due to the ROI attenuator were carried out in terms of integral dose,[4,15,16] there have been no detailed studies of organ and effective dose reduction for CBCT and interventional fluoroscopic procedures with the ROI attenuator. For this work, we used EGSnrc

---

*Address all correspondence to: Zhenyu Xiong, E-mail: [zhenyuxi@buffalo.edu](zhenyuxi@buffalo.edu)

Monte Carlo code to calculate the organ and effective dose reduction with an ROI attenuator for these procedures.

## 2 Materials and Methods

### 2.1 Monte Carlo Method for X-Ray Beam Modeling

To generate the spectra used for CBCT and interventional fluoroscopic procedures with/without the ROI attenuator, the x-ray tube of the Toshiba Infinix C-Arm System was modeled by BEAMnrc/EGSnrc code. All parts of the x-ray tube including tube target design, beam collimation and beam filtration systems; incident electron angle and energy were simulated according to the manufacturer's specifications, and we were able to obtain more specific matching of the x-ray beam characteristics including energy and direction than if we had used a standard spectrum generator. We used the XTUBE component module (CM) of the BEAMnrc code library to simulate the tube anode, with a target material of tungsten–rhenium (WRe) and an anode angle of 11 deg. The incident electron energy was simulated using a constant potential with no ripple. The SLABS CM was employed to simulate the beryllium (Be) window, inherent filtration, and added filtration. Additional aluminum filtration was adjusted to match the half-value layer (HVL) with that measured for the beam. The CIRCAPP CM was employed to simulate the ROI attenuator with different dimensions and materials. The JAWS CM was set up to simulate two pairs of lead collimators, which can adjust the FOV.

To enhance photon fluence production and increase the simulation efficiency, we used the variance reduction technique known as directional bremsstrahlung splitting (DBS) with a splitting number of 2000 and the Russian Roulette (RR) was set outside the DBS field of interest. The anode bremsstrahlung cross-section enhancement was increased by a factor equal to 200. In all simulations, the photon energy cut-off (global PCUT) was set to 10 keV for range rejection.[17] Material data were generated by the PEGS4 code developed at National Research Council.[18] We also turned on the following low-energy physics options for accurate simulation: electron impact ionization, bound Compton scattering, photoelectron angular sampling, atomic relaxation, Rayleigh scattering, and simple bremsstrahlung angular sampling. The NIST data were used for all bremsstrahlung cross-section simulations and XCOM was used for photoabsorption and Rayleigh-scattering total

cross sections. The EXACT boundary crossing algorithm (BCA) was used, which utilizes a single elastic scattering mode for electron transport as soon as they are within a distance from the boundary given by the EGSnrc input "skin depth for BCA."[19] A "skin depth for BCA" of three elastic mean free paths was used and has been found to give peak efficiency in this case. The PRESTA-II electron-step algorithm was employed to calculate lateral and longitudinal corrections. A parallel rectangular monoenergetic beam of $5 \times 10^9$ electrons is incident on the target.

A phase space (PHSP) file contains the spatial and directional information with energies for all x-ray photons in the beam and was determined at a distance of 24 cm from the focal spot, which is greater than the distance of the last component within the x-ray tube module, including the ROI attenuator. After the last components of the tube and collimator, the PHSP file describing the beam characteristics can be regenerated at any source-to-skin distance. We have used the PHSP files to find the spectra and percent-depth dose (PDD) and HVL of the simulated beam. The x-ray spectra that were simulated using the BEAMnrc on the central axis of the beam were compared to those calculated by SpekCalc.[20] To verify the matching of the PHSP file and actual spectra, we compared the PDD calculated by EGSnrc with the PDD measured for the Toshiba x-ray tube using a 0.6-cm$^3$ Farmer chamber (model NE2507/3A, Nuclear Enterprises, Fairchild, New Jersey) in a solid-water phantom at 80 kVp. Both PDD curves were normalized to their maximum value.

The x-ray photons in the PHSP file were transported to the voxel phantom generated with the anthropomorphic phantom CT data in DOSXYZnrc[19] user code. After the BEAMnrc simulations were completed, PHSP file were used to run DOSXYZnrc user code in order to determine the dose deposited per simulated particle in the phantom. In each DOSXYZnrc simulation, the number of histories run was equal to the number of photons stored in the PHSP file. Table 1 shows the number of photons included in every PHSP file. We used a source type 8 (phase-space source from multiple directions) to simulate the rotational irradiation of the CBCT scans and source type 2 (full phase-space source file) to simulate every exposure of the interventional procedures. Table 1 shows the PHSP file sizes and time required to simulate the sources in BEAMnrc. It also shows the time required to simulate the organ and effective dose in EGSnrc.

**Table 1** Details of the single-projection (80 kVp) and 407-projection CBCT (120 kVp) EGSnrc simulations including the number of photons in the PHSP files, the PHSP file sizes, time required for BEAMnrc simulation, and time required for DOSxyznrc simulation. All simulations were done on a computer with an Intel i5-4690 K 3.5 GHz CPU.

| | 80 kVp | | 120 kVp | | | | | | |
|---|---|---|---|---|---|---|---|---|---|
| | $p = 12\%$, $t = 0.7$ mm | | $p = 12\%$ | | | | | $t = 0.7$ mm | |
| | Without ROI | With ROI | Without ROI | $t = 0.35$ mm | $t = 0.7$ mm | $t = 1.05$ mm | $t = 1.4$ mm | $p = 24\%$ | $p = 36\%$ |
| Number of photons | $1.2 \times 10^9$ | $8.9 \times 10^8$ | $3.1 \times 10^9$ | $2.6 \times 10^9$ | $2.5 \times 10^9$ | $2.4 \times 10^9$ | $2.3 \times 10^9$ | $2.6 \times 10^9$ | $2.7 \times 10^9$ |
| PHSP file size (GB) | 34.2 | 24.8 | 85.2 | 75.2 | 70.7 | 67.7 | 65.4 | 72.8 | 75.2 |
| BEAMnrc simulation time (h) | 101 | 95 | 148 | 140 | 139 | 139 | 138 | 140 | 141 |
| DOSxyznrc simulation time (h) | 0.5 | 0.3 | 22.7 | 18.2 | 15.8 | 14.4 | 13.1 | 17.3 | 18.9 |

Note: $t$ is ROI attenuator thickness, $p$ is the percentage of aperture size to area of the FOV.

## 2.2 Region-of-Interest Attenuator and Phantom Geometry Modeling

The ROI attenuator in the x-ray tube of the Toshiba Infinix C-Arm System in our laboratory was modeled in EGSnrc. The ROI attenuator is a rectangular sheet of copper with a thickness of 0.7 mm and a circular aperture that is 12% of the area of the FOV of the $30 \times 30$ cm detector at 120-cm source to image-receptor distance (SID). This thickness was chosen since it absorbs 91.9% of the beam with a 3.1-mm Al HVL at 80 kVp as typically used for digital angiography (DA) exposures and 75.4% with a 120-kVp, 4.5 mm-Al HVL beam as used for CBCT. This provides a good compromise between dose reduction and acceptable noise in the periphery as demonstrated in several studies.[4,21] The greater the copper thickness, the greater will be the quantum noise in the image area outside of the ROI. This noise can be reduced by spatially variable temporal filtering when appropriate.[4] The size of the aperture selected is dependent on the needs of a procedure and the 12% aperture was found to be suitable for neurointerventional procedures. The smaller the aperture, the smaller is the region of high image quality, but the less will be the scattered radiation generated and the higher will be the signal–to-noise ratio in the ROI. To investigate the effect on dose of the ROI attenuator aperture size, ROI attenuators with circular apertures encompassing 12%, 24%, and 36% of the FOV and a copper thickness of 0.7 mm were modeled. To investigate the effect of attenuator thickness, ROI attenuators with thicknesses of 0.35, 0.7, 1.05, and 1.4 mm and with circular apertures encompassing 12% of the FOV were also modeled separately. Table 2 shows the primary beam attenuation for the different thicknesses of Cu attenuator used for both 80 and 120 kVp.

To validate the reliability of our simulation, we compared the entrance dose distribution calculated with EGSnrc to that measured with Gafchromic™ XR-QA2 film (Ashland, New Jersey) for DA exposures on a solid-water block phantom. The phantom's dimensions were 30 cm $\times$ 30 cm $\times$ 20 cm thick, and the beam size was 30 cm square at 120-cm SID. The beam peak voltage was set to 80 kVp (HVL = 3.1 mm Al), tube current was 80 mA, exposure time was 10 ms, frames/second was 15, scan time was 50 s, and the 1.8-mm Al system beam filter was used. The distance from source to phantom surface was 54 cm, which was the interventional reference point. The dose–response curve of the film was determined using a calibrated 0.6-cm³ Farmer type ionization chamber. We put the film at the same location at the entrance surface of the phantom and did the same DA exposure with and without the ROI attenuator. To get the dose distribution, the exposed films were digitized with an HP Photosmart 7510 flatbed scanner 24 h after exposure.

**Table 2** Primary beam attenuation for the different thicknesses (*t*) of Cu ROI attenuator used at 80 and 120 kVp. For both kVps, 1.8 mm Al was selected on the imaging system as the added filtration.

|  | *t* = 0.35 mm | *t* = 0.7 mm | *t* = 1.05 mm | *t* = 1.4 mm |
|---|---|---|---|---|
| 80 kVp, 3.1-mm AL HVL (%) | 82.8 | 91.9 | 95.6 | 97.3 |
| 120 kVp, 4.5-mm AL HVL (%) | 61.5 | 75.4 | 82.7 | 87.5 |

For organ and effective dose calculation in our simulations of CBCT and interventional procedures, the Zubal CT torso + head computational phantom[22] was used. This phantom was developed based on a whole-body CT scan of an adult male whose radiosensitive organs and tissues, including the eye lens, were individually segmented. The weight and the height of the patient model were 70 kg and 178 cm, respectively. The torso + head phantom consists of isotropic voxels with dimensions of 4 mm. Each voxel in the phantom was assigned a tissue type, described by elemental composition and mass density. An .egsphant file was constructed to describe the Zubal CT torso + head phantom by using a Visual C++ program. This file includes the coordinate, material, and density information. When calculating the skin dose, the 4-mm voxels might underestimate the dose because of attenuation when the skin thickness is less. Our calculations show that this would amount to a difference of about 1.5% if the skin were only 1.5 mm.

## 2.3 Organ and Effective Dose Calculation for CBCT Scans

For the CBCT scans, we used the LCI-Middle protocol on the Toshiba Infinix system with a source to isocenter distance of 69 cm, a field size of $30 \times 30$ cm at 120-cm SID, a peak voltage of 120 kVp and 4.5-mm Al HVL, a tube current of 4.56 mAs per frame, a rotational range of 203 deg (from right anterior oblique 101 deg to left anterior oblique 102 deg), and 407 frames. Monte Carlo simulated CBCT scans were performed in the head and in the heart position of the thorax with the centerline of the phantom placed at rotational isocenter. To investigate the effect of different locations of the CBCT scan, three different axial positions were used for the head scans ($Z = 6$ cm, $Z = 7.5$ cm, and $Z = 9$ cm from the top of the head) and two were used for the thorax scans ($Z = 37.6$ cm and $Z = 42.6$ cm), as shown in Fig. 1.

## 2.4 Organ and Effective Dose Calculation for Interventional Fluoroscopy Procedures

We also simulated a neuro- and a cardiac-interventional fluoroscopic procedure on our Toshiba Infinix C-Arm System using geometry and exposure parameters similar to clinical procedures. All of the projection geometry and exposure parameters for every x-ray pulse used in these procedures were saved from the imaging system digital Controller Area Network (CAN bus) messages in a log file by the real-time skin-dose tracking system (DTS)[23] were previously developed. After the procedures, we used MATLAB code to read data from the log files and to automatically generate definition files in the format used by EGSnrc. Usually, there are thousands of rows of parameters in the log file in an interventional fluoroscopy procedure because some parameters, like projection angle, focus-skin distance, beam field size, and beam position, are always changing. Thus, we grouped data with similar technique parameters to reduce calculation time. The efficiency and accuracy of this grouping method has been demonstrated in previous studies.[24–26]

As others have done in order to calculate absolute organ doses from the Monte Carlo simulation, a calibration factor was determined.[27–29] The calibration factor Fc is a function of beam energy $E$ and is given by

$$(\mathrm{Fc})_E = (D_{\mathrm{meas}})_E / (D_{\mathrm{MC}})_E, \qquad (1)$$
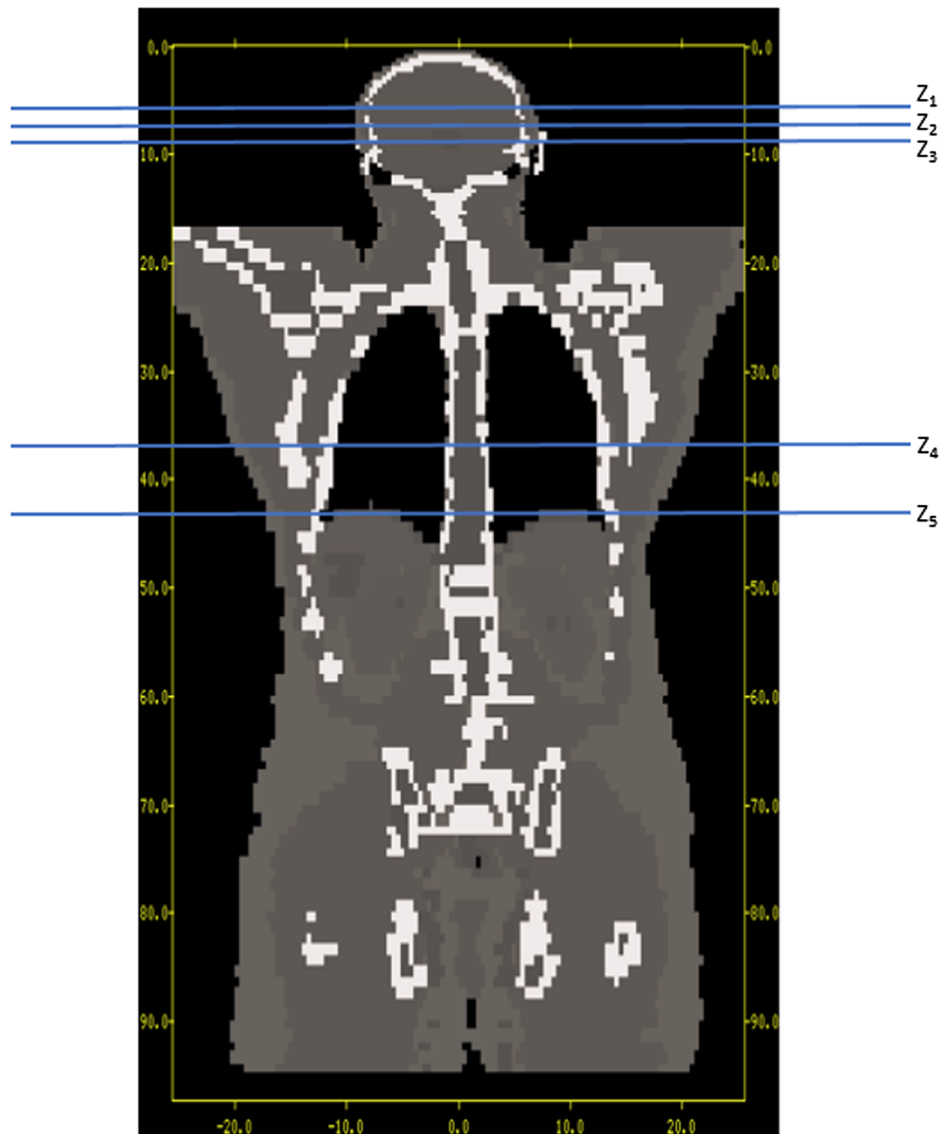
**Fig. 1** Three axial positions of the isocenter for CBCT scans in the head ($Z_1 = 6$ cm, $Z_2 = 7.5$ cm, and $Z_3 = 9$ cm) and two axial positions of the isocenter for CBCT scans in the heart position of the thorax ($Z_4 = 37.6$ cm and $Z_5 = 42.6$ cm) for the Monte Carlo simulations in order to investigate the variation with location. ($Z$ is the distance from the top of the head.)

where $D_{meas}$ is the dose in Gy per mAs measured with the ionization chamber placed free in-air at the isocenter determined during a DA exposure and during a CBCT scan, whereas $D_{MC}$ is the Monte Carlo dose in Gy/particle (averaged over the beam spectrum), which was determined from a simulation of the same exposures in EGSnrc. Calibration factors were determined for each tube voltage used. The absolute dose to a given voxel in a phantom is calculated from the simulated dose value as

$$D_{absolute} = D_{simulated} * \text{Fc} * \text{mAs}, \qquad (2)$$

where $D_{simulated}$ is the Monte Carlo simulated dose in Gy/particle, $D_{absolute}$ is the calculated absolute dose in Gy in that voxel, and mAs is the total mAs used for the given exposure. The organ doses were calculated by averaging the dose calculated in all voxels in that organ. In this study, the effective dose was calculated using the tissue weighting factors according to ICRP 103 after we calculated individual organ doses. Although the dose to the eye lens does not contribute to the effective patient dose, it is considered individually because of the increasing concern for cataract formation. Recent studies have suggested that the dose threshold for cataracts is lower than previously believed or even that the effect is stochastic without a threshold.[30–32]

## 3 Results

### 3.1 *Validation of the Monte Carlo Model*

Comparison of the SpekCalc simulated x-ray spectrum with the spectrum simulated using the EGSnrc/BEAMnrc on the central axis of the beam is shown in Fig. 2. The characteristic peaks are shown superimposed on a continuous spectrum. In general, the agreement between the shape of the bremsstrahlung spectra acquired from the EGSnrc/BEAMnrc simulation and the SpekCalc spectrum generator is good.
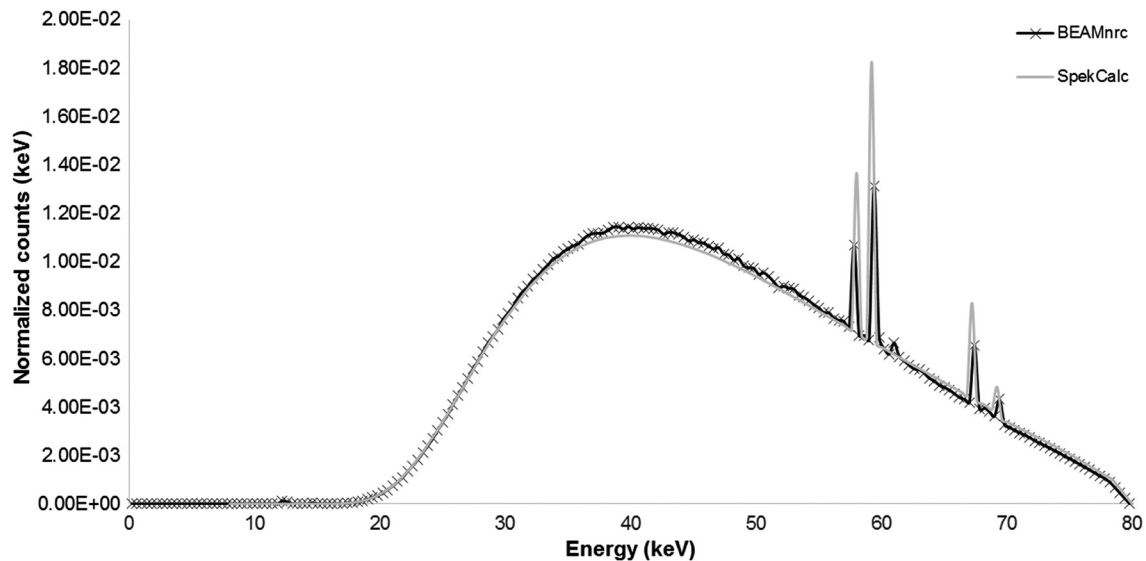
**Fig. 2** X-ray spectrum at 80 kVp using BEAMnrc for simulation of the Toshiba Infinix beam compared with the spectrum generated by SpekCalc.
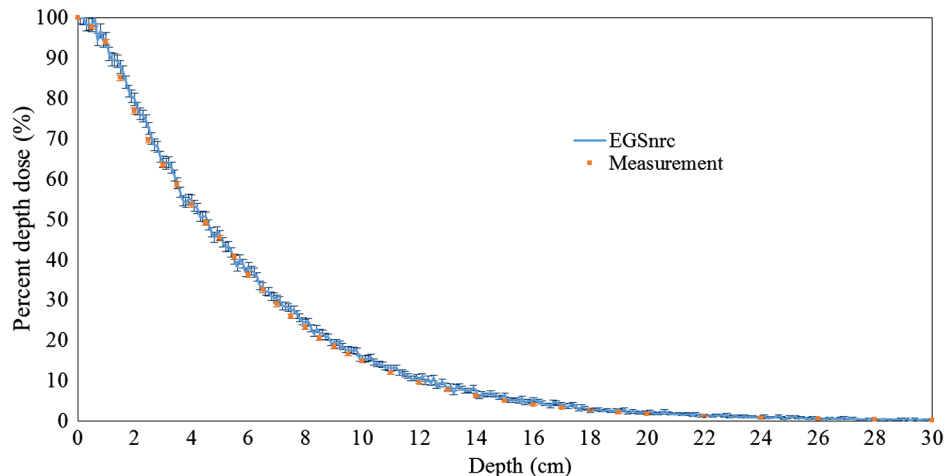


**Fig. 3** Comparison of the 80-kVp PDD curve simulated by EGSnrc and that measured in solid water using a Farmer ionization chamber. In the EGSnrc simulation, a statistical uncertainty of less than ±2% was achieved for a depth from 0 to 5 cm.

Figure 3 shows the comparison of the PDD curve produced by the EGSnrc/BEAMnrc simulation and experimental measurement with the 0.6-cm$^3$ Farmer chamber. The simulated transmission curve is slightly higher than the measured transmission curve for all thicknesses but the difference was generally less than 5%. The HVLs for the EGSnrc/BEAMnrc simulation and measurement with the ionization chamber are 3.2 and 3.1 mm Al, respectively.

### 3.2 Surface Dose Distribution for Solid-Water Block Phantom

Figures 4(a) and 4(b) show the Gafchromic film after exposure on the surface of the solid-water phantom for a single DA projection without (a) and with (b) the ROI attenuator and Figs. 4(c) and 4(d) show the corresponding color-coded dose distribution calculated by EGSnrc without (c) and with (d) the ROI attenuator. The ROI attenuator thickness and opening size of the FOV

is the same as the ROI attenuator in our C-arm system (0.7 mm Cu and 12% FOV). The nonuniformity of dose distribution in the anode–cathode direction (horizontal) is due to the Heel effect.

Figure 5 shows the entrance surface dose profiles at the midline of the entrance field dose distribution calculated by EGSnrc. It shows that the average surface dose reduction in the ROI opening is about 10.5% resulting from the reduced backscatter from the area outside the ROI. The average relative surface dose reduction outside the ROI opening is about 86%. The primary beam reduction due to attenuation by the copper is about 92% and the additional radiation is due in part to backscatter from the higher intensity ROI. Figure 5 also shows the line dose profiles obtained along the midline of the entrance field dose distribution with the ROI attenuator simulated by EGSnrc and validated by a Gafchromic film measurement. The result shows good agreement between Monte Carlo simulation and film measurement in both the ROI and the periphery.
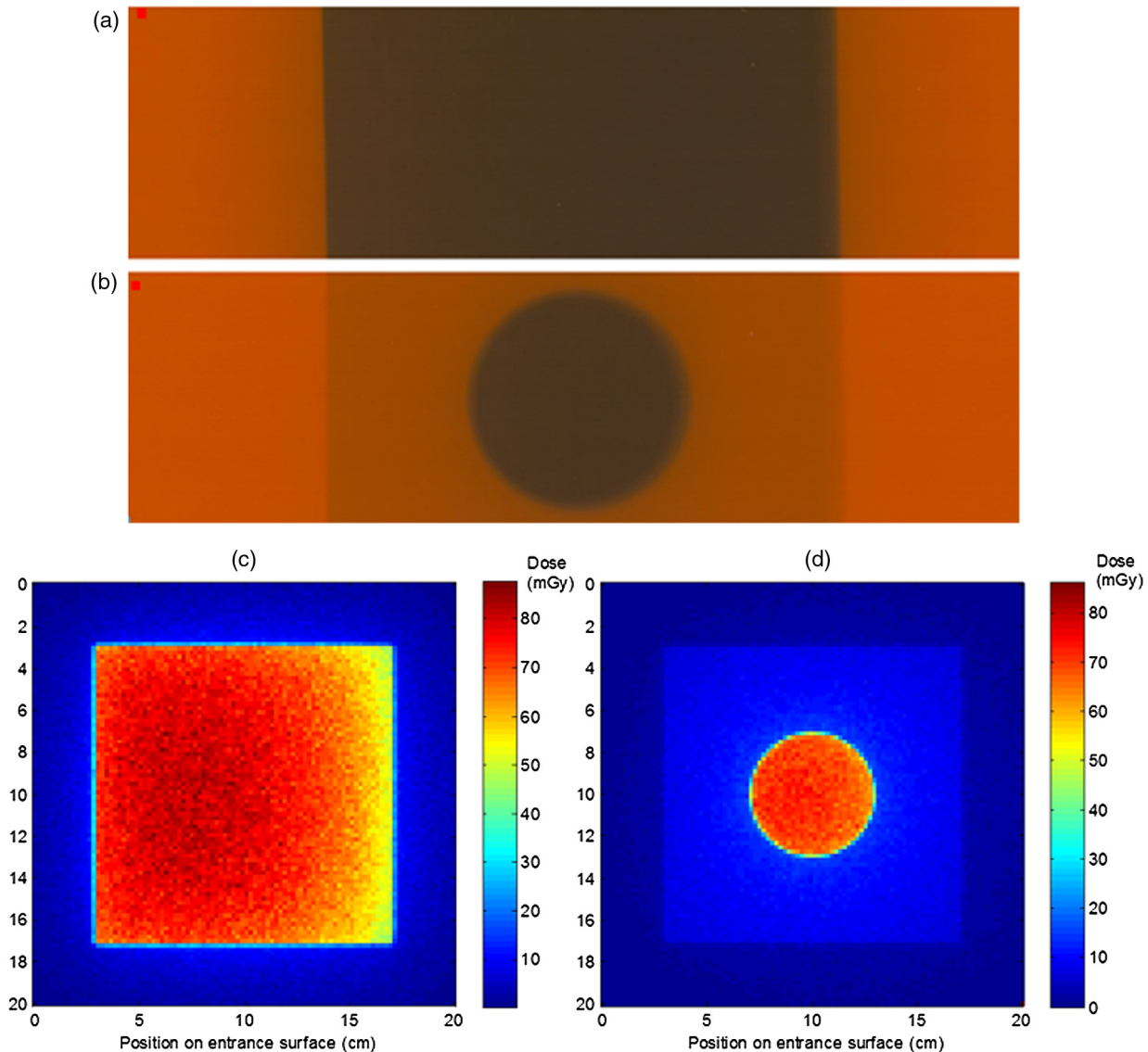
**Fig. 4** The dose distribution on the entrance surface of the solid-water block for a DA exposure as seen on the Gafchromic film (a) without and (b) with the ROI attenuator and the color-coded distribution calculated by EGSnrc (c) without and (d) with the ROI attenuator. The ROI attenuator was a copper sheet with a thickness of 0.7 mm and a circular aperture which was 12% of the FOV of the 30 × 30 cm detector at 120-cm SID.

### 3.3 Organ Dose and Effective Dose Reduction in CBCT Procedures

Figure 6 shows the dose reduction effect of the ROI attenuator in an LCI-Middle protocol CBCT procedure on the Toshiba Infinix system at the patient's head location. Without the ROI attenuator, the average brain dose is about 211 mGy, whereas the thyroid and spinal cord received the lowest dose of about 12 mGy; the effective dose of the CBCT procedure was 8.1 mSv. As expected, the organ and effective dose reduction was greater with increasing attenuator thickness when the ROI attenuator is added in the tube. For example, the thyroid dose can be reduced from 11.7 mGy without the ROI attenuator to 4.1 mGy when applying a 1.4-mm-thick ROI attenuator and opening size of 12% FOV [Fig. 6(a)]. This is a relative dose reduction of 65%, as shown in Fig. 6(a).

The effect of the ROI attenuator also depends on the ROI opening size. The organ and effective dose were reduced more effectively with a smaller opening size (from 36% to 12% of the FOV), as shown in Fig. 6(b). For instance, the brain dose can be reduced from 174 mGy when applying an ROI attenuator with 0.7-mm thickness and opening size of 36% FOV to 117 mGy when applying an ROI attenuator with the smaller opening size of 12% and the same thickness. This corresponds to a relative reduction of 33%, as shown in Fig. 6(b).

Figure 7 shows organ and effective dose reduction with the ROI attenuator for neuro-CBCT procedures with different axial positions. As the axial position moved from 9 to 6 cm, an obvious difference in organ dose can be seen for the thyroid, the spinal cord, and the salivary glands, whereas the changes of organ dose for the brain and eye lens were minor. For example, with the ROI attenuator, the salivary glands dose was reduced from 80 to 28 mGy when the axial position changed from 9 to 6 cm; however, the brain dose increased only from 117 to 131 mGy. As one might expect, the further up the
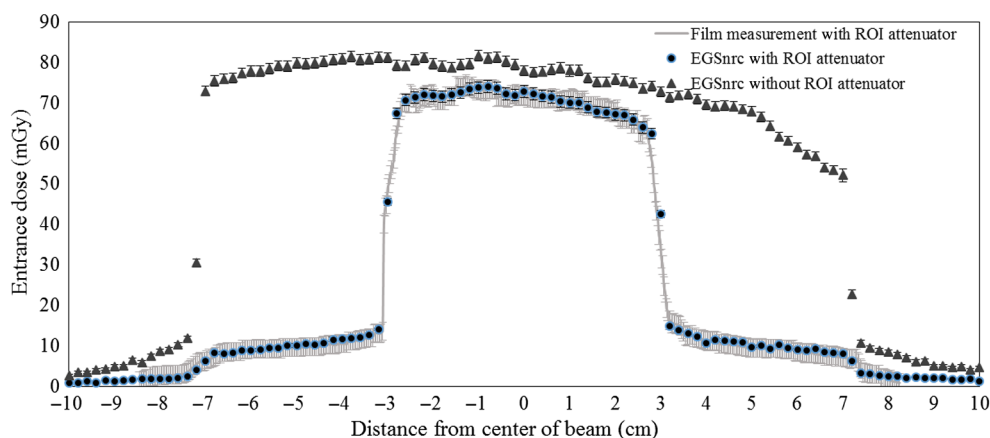
**Fig. 5** Line profiles calculated by EGSnrc along the midline of the entrance field dose distribution in the anode–cathode direction with the anode on the right with and without the ROI attenuator and line dose profile measured by Gafchromic film with the ROI attenuator. (Profiles are taken from the distributions shown in Fig. 4).
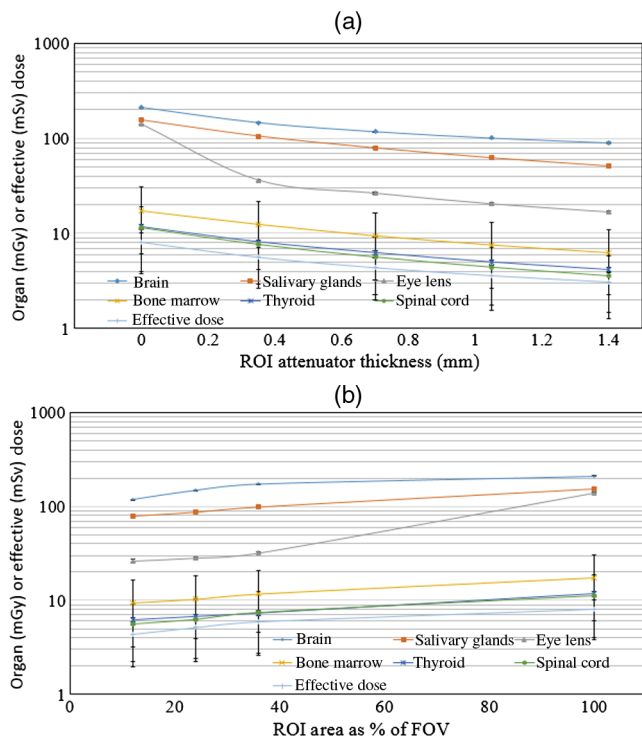


**Fig. 6** Organ and effective doses determined for neuro-CBCT procedures using EGSnrc simulation with the Zubal phantom as a function of the ROI attenuator thickness and ROI opening size as a percent of the FOV. The tube peak voltage was set to 120 kVp and axial position was 9 cm. (a) Organ and effective doses shown as a function of ROI attenuator thickness for an ROI 12% of the FOV and (b) organ and effective doses shown as a function of ROI opening size as a percentage of the FOV for an ROI thickness of 0.7-mm Cu.

scan is in the patient's head, the lower is the organ dose for the salivary glands, thyroid, and spinal cord, and the higher the organ dose is for the brain. Organs like the eye lens are always located in the attenuated region of the beam with the ROI attenuator when the axial position is moved, and thus, there was very little change in dose to the eye lens. With the ROI attenuator, the effective dose was reduced from 4.4 to 3.3 mSv when the axial position moved from 9 to 6 cm. For a thoracic CBCT scan with

the ROI attenuator, the effective dose was reduced from 17.2 to 14.9 mSv when the axial position moved from 42.6 to 37.6 cm.

Figure 8 shows the dose reduction effect of the ROI attenuator in an LCI-Middle protocol CBCT procedure on the Toshiba Infinix system at the patient's heart position of the thorax. Without the ROI attenuator, the radiosensitive organs like lung, stomach, and liver received relatively high dose because they were located in the high exposure area. After the ROI attenuator was added to the beam, the dose for these organs was reduced significantly. For instance, the lung dose can be reduced from 84 mGy without the ROI attenuator to 31 mGy when adding an ROI attenuator with 1.4-mm thickness and opening size 12% of the FOV. The organ and effective dose reduction was greater with increasing attenuator thickness when an ROI attenuator is added. For most of the important radiosensitive organs, the dose reductions are about 30% to 35% with the 0.35-mm thickness ROI attenuator compared to about 60% to 65% with the 1.4-mm thickness ROI attenuator. Also, the effective dose reduction increases from 32% to 62% when the thickness of ROI attenuator is increased from 0.35 to 1.4 mm.

Figure 9 shows how the dose reduction effect of the ROI attenuator depends on the opening size. As expected, the organ and effective dose were reduced more effectively with the smaller opening size (from 36% to 12% of the FOV). For instance, the liver dose can be reduced from 74 mGy without the ROI attenuator to 50 mGy with the 36% FOV opening size and to 38 mGy with the 12% FOV opening size. For most of the important radiosensitive organs, the dose reductions are about 30% with the 36% FOV opening size compared to about 45% to 50% with the 12% FOV opening size. Also, the effective dose reduction increases from 30% to 47% when the opening size of the ROI attenuator is decreased from 36% to 12% of the FOV.

### 3.4 Organ and Effective Dose Calculation in Interventional Fluoroscopy Procedures

Figure 10 shows the dose reduction effect of an ROI attenuator with 0.7-mm thickness and an opening size of 12% FOV in a simulated neurointerventional procedure. In this procedure, most of the organ dose reductions were about 55% to 60%.
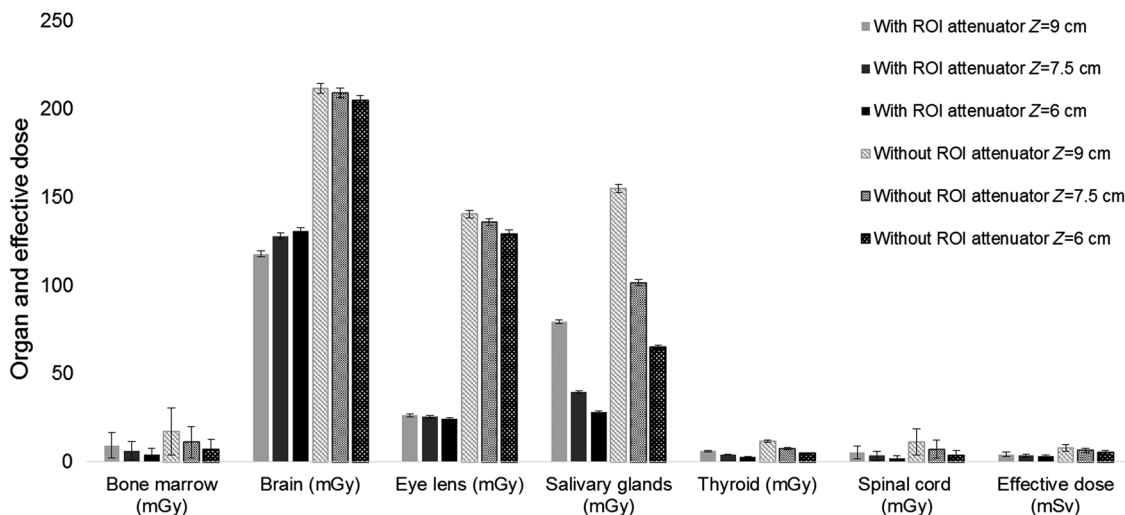
**Fig. 7** Organ and effective doses determined for neuro-CBCT procedures using EGSnrc simulation with the Zubal phantom for different axial positions of the beam. The tube peak voltage was set to 120 kVp and axial position was 6, 7.5, and 9 cm.
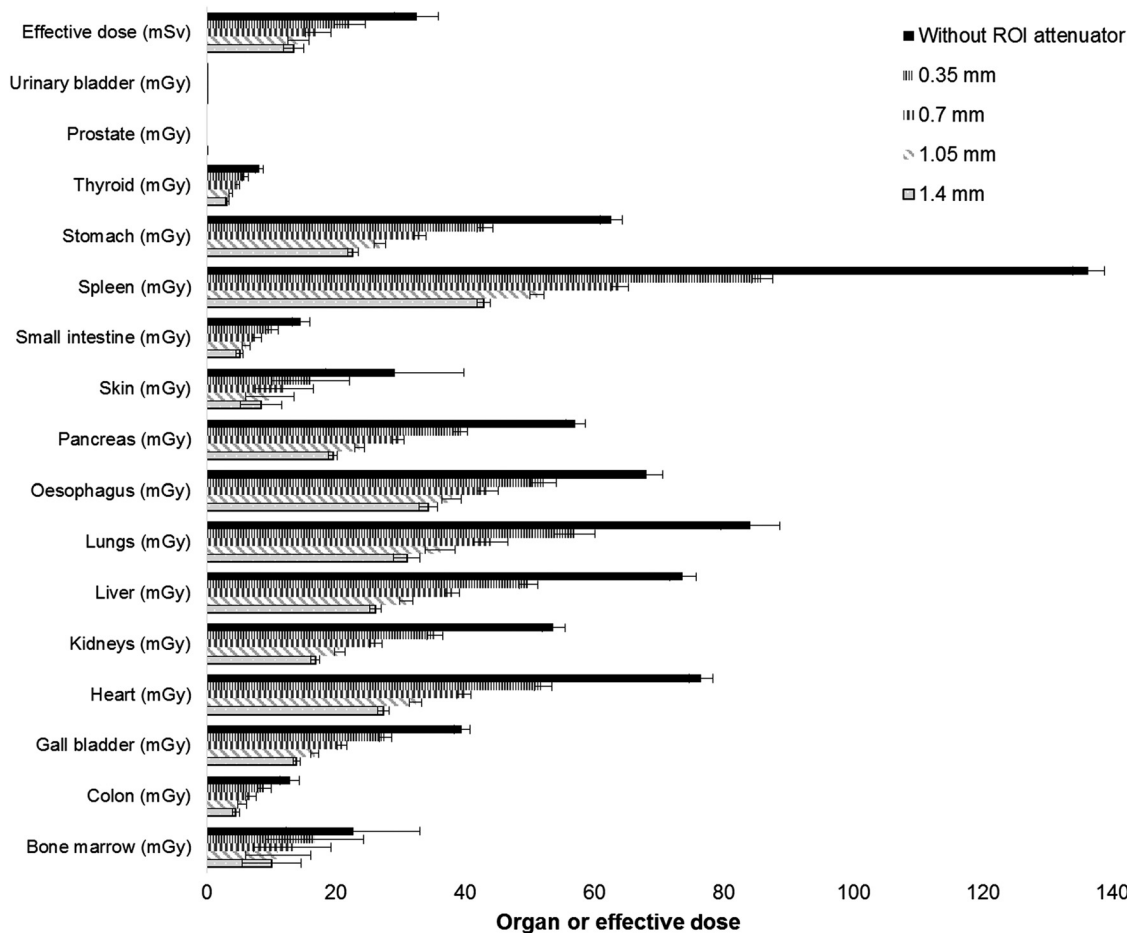


**Fig. 8** Organ and effective doses determined for thoracic CBCT procedures using EGSnrc simulation with the Zubal phantom as a function of the ROI attenuator thickness. The tube peak voltage was set to 120 kVp and axial position was 42.6 cm.

For example, the salivary glands dose decreased from 294 to 123 mGy with the ROI attenuator added, resulting in a dose reduction of about 58%. The effective dose also decreased about 58% from 36.6 to 15.9 mSv.

Figure 11 shows the dose reduction effect of an ROI attenuator with 0.7-mm thickness and an opening size of 12% FOV in a simulated cardiac interventional procedure. In this procedure, the dose reductions for most of the radiosensitive organs were
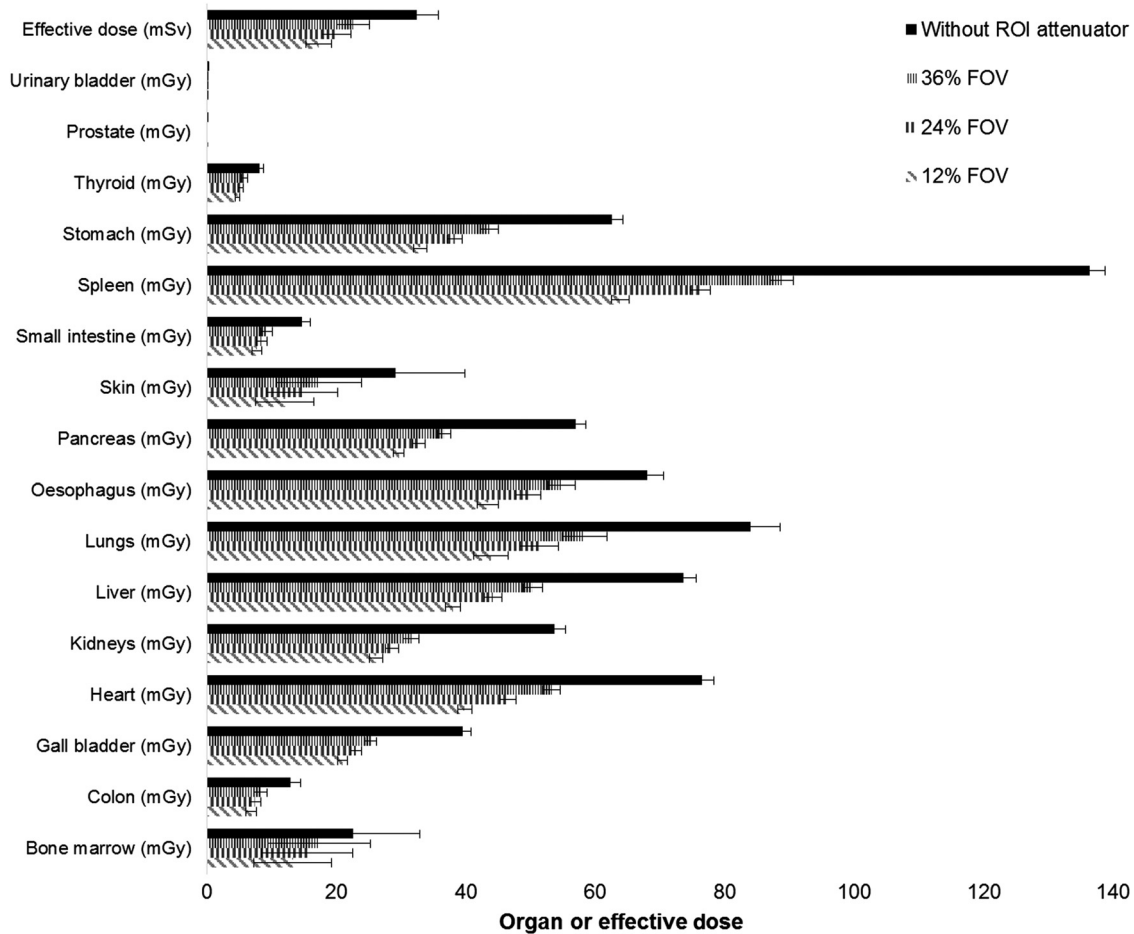
**Fig. 9** Organ and effective doses determined for thoracic CBCT procedures using EGSnrc simulation with the Zubal phantom as a function of the ROI opening size for 0.7-mm-thick Cu at an axial position of 42.6 cm.
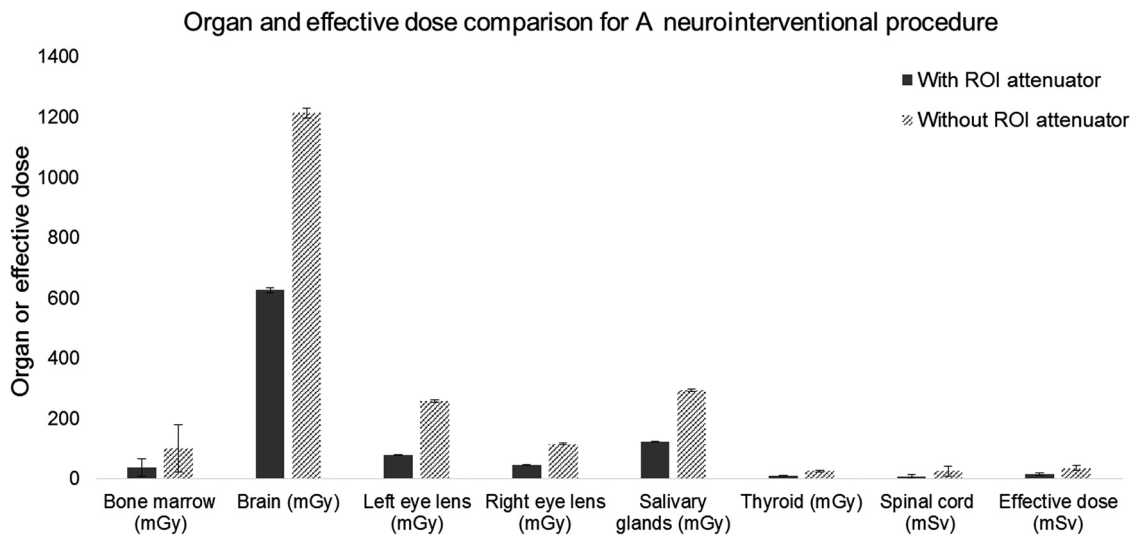


**Fig. 10** Organ and effective dose comparison for a simulated neurointerventional procedure with and without an ROI attenuator (0.7-mm-thick Cu, 12% FOV).

about 65% to 70%. For example, the lung dose decreased from 55 to 16 mGy with the ROI attenuator added, for a dose reduction of about 71%; the stomach dose decreased from 41 to 17 mGy with the ROI attenuator added, for a dose reduction of about 59%. The effective dose decreased from 22.7 to 7.8 mSv, for a reduction of about 66%.
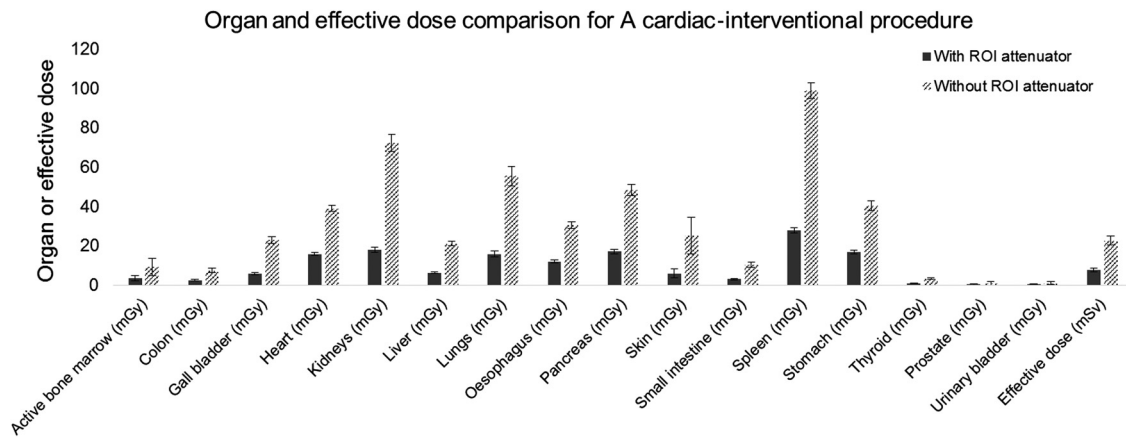
**Fig. 11** Organ and effective dose comparison for a simulated cardiac interventional procedure with and without an ROI attenuator (0.7-mm-thick Cu, 12% FOV).

## 4 Discussion

It is important to minimize patient dose to minimize the radiation risk during CBCT scans and interventional procedures.[33] Dose management techniques include the use of intermittent fluoroscopy (short bursts of beam-on time)[34] and positioning the image receptor as close to the patient's body as possible while maximizing the distance from the x-ray tube.[35] Collimating the x-ray beam to include only the anatomic ROI can substantially decrease patient dose but with a loss of visualization of the peripheral region. To maintain visualization over the entire FOV while gaining much of the dose reduction benefit of collimation, we developed a method of using an ROI attenuator to reduce dose in regions of lower interest and preserve high image quality in the region of interventional activity.

This study verified the substantial dose reduction benefit of using ROI attenuators for CBCT scans and interventional procedures and evaluated the dependence of organ and effective dose on attenuator thickness (Fig. 6), ROI opening size (Figs. 8 and 9), and axial or Z position of the rotational isocenter (Fig. 7). The dose reduction differences with changes in beam axial position when using the attenuator were dependent on the individual organ location and were greater for the smaller organs because they have a higher likelihood of being entirely located in the attenuated area of the ROI attenuator than the larger organs. For instance, with the ROI attenuator, when the axial position of the neuro-CBCT scan moved from 9 to 6 cm, the salivary glands' dose was reduced much more than the brain dose. The importance of the location of different organs on their dose reduction effect is shown in Figs. 6 and 7. When the ROI attenuator with 0.7-mm-thick Cu and a circular aperture that was 12% of the FOV was added, the reduction of eye lens dose is about 81%, which is greater than other organs' dose reduction (about 40% to 45%). This is because the eye lens was always located in the attenuated area of the ROI attenuator. Because of this, when the ROI attenuator is added, the dose reduction of the lens changed very little when the axial position changed.

Moritake et al.[36] reported an average dose to the patients' eyes lens of 380 mGy, with a maximum of 2079 mGy during cerebral embolizations, which is about 4 times the new threshold level of 500 mGy recommended by the ICRP. For our simulated neurointerventional procedure, we showed a lens dose reduction

of about a 60% with the ROI attenuator so that the average eye lens dose in Moritake's survey could be reduced to about 150 mGy, well below the-500 mGy threshold.

The neuro- and the cardiac-interventional fluoroscopic procedures in this study were simulated with similar geometry and exposure parameters to clinical procedures. However, there is a large variability between actual procedures due to differences in the complexity of the case and the experience of the interventionist, and thus the total dose distribution may differ with individual clinical cases. Also, the dose reduction in our simulated interventional procedures will likely be overestimated since we applied the ROI attenuator for the whole procedure, whereas the interventionist would likely apply the attenuator selectively during a procedure when concentrating on the activity is a small region. However, since the most of the dose to the patient is given during the interventional activity after the target region has been localized, the dose reduction calculated in our simulated interventional procedures should not be a large overestimate. Using our grouping method for exposure events during the interventional procedure, the Monte-Carlo dose calculation time was greatly reduced while maintaining high accuracy. For instance, in the simulated neurointerventional procedure, the simulation time was reduced from several tens of days (estimated) if the dose was calculated for every exposure pulse to about 10 h with EGSnrc by grouping and such calculations would likely be done after a procedure. We expect that different "rules" for grouping may be appropriate depending on the type of procedure in order to optimize the reduction of calculation time while maintaining accuracy.

Detailed evaluation of the acceptability of a given ROI aperture size or attenuator thickness for a particular procedure is beyond the scope of this paper and has been investigated by others.[37,38] Selection of these details for the ROI attenuator will be somewhat subjective and depend on the procedure type and the capabilities of the imaging system for display brightness equalization or noise reduction processing.

## 5 Conclusions

In this work, we quantitatively evaluated the potential organ and effective dose reductions of ROI imaging applied to CBCT and interventional fluoroscopic procedures. For an ROI attenuator made with 0.7-mm-thick Cu and a circular aperture that was 12% of the FOV, the results of Monte-Carlo calculations showed a reduction in the dose to most organs of 45% to 50% and in

effective dose of about 46% compared to the dose in standard neuro-and thoracic-CBCT scans without the ROI attenuator; a reduction in dose for most radiosensitive organs of 55% to 60% (65% to 70%) and in effective dose of 58% (66%) compared to the dose in a simulated neuro- (cardiac) interventional fluoroscopic procedure without the ROI attenuator was determined. In particular, the reduction in eye lens dose can be up to 80% compared to the dose in standard neuro-CBCT without the ROI attenuator. The dependence of dose reduction on the ROI attenuator thickness, the opening size of the ROI, the beam position, and the location of the different organs was also evaluated. This work demonstrates the effectiveness of ROI imaging in reducing patient radiation dose.

## Disclosures

## Acknowledgments

## References

1. F. A. Stewart et al., "ICRP statement on tissue reactions and early and late effects of radiation in normal tissues and organs—threshold doses for tissue reactions in a radiation protection context," *Ann. ICRP* **41**(1–2), 1–322 (2012).
2. J. Valentin, "The 2007 recommendations of the International Commission on Radiological Protection," *Ann. ICRP* **37**, 1–332 (2007).
3. S. Rudin and D. R. Bednarek, "Region-of-interest fluoroscopy," *Med. Phys.* **19**, 1183–1189 (1992).
4. S. N. S. Vasan et al., "Dose reduction in fluoroscopic interventions using a combination of a region of interest (ROI) x-ray attenuator and spatially different, temporally variable temporal filtering," *Proc. SPIE* **8668**, 86683Y (2013).
5. S. Rudin, D. R. Bednarek, and C. H. J. Yang, "Real-time equalization of region-of-interest fluoroscopic images using binary masks," *Med. Phys.* **26**(7), 1359–1364 (1999).
6. S. Rudin et al., "Applications of region-of-interest imaging techniques in neurointerventional radiology," *Radiology* **199**, 870–873 (1996).
7. U. Missler et al., "Three-dimensional reconstructed rotational digital subtraction angiography in planning treatment of intracranial aneurysms," *Eur. Radiol.* **10**(4), 564–568 (2000).
8. A. Hochmuth, U. Spetzger, and M. Schumacher, "Comparison of three dimensional rotational angiography with digital subtraction angiography in the assessment of ruptured cerebral aneurysms," *Am. J. Neuroradiol.* **23**(7), 1199–1205 (2002).
9. J. K. Song et al., "Simultaneous bilateral internal carotid artery 3D rotational angiography," *Am. J. Neuroradiol.* **25**(10), 1787–1789 (2004).
10. T. Sugahara et al., "Comparison of 2D and 3D digital subtraction angiography in evaluation of intracranial aneurysms," *Am. J. Neuroradiol.* **23**(9), 1545–1552 (2002).
11. A. Hochmuth, U. Spetzger, and M. Schumacher, "Comparison of three-dimensional rotational angiography with digital subtraction angiography in the assessment of ruptured cerebral aneurysms," *Am. J. Neuroradiol.* **23**(7), 1199–1205 (2002).
12. J. K. Song et al., "Simultaneous bilateral internal carotid artery 3D rotational angiography," *Am. J. Neuroradiol.* **25**(10), 1787–1189 (2004).
13. J. C. V. D. Berg et al., "Using three-dimensional rotational angiography for sizing of covered stents," *Am. J. Roentg.* **178**(1), 149–152 (2002).
14. RN Chityala et al., "Region of interest (ROI) computed tomography (CT): comparison with full field of view (FFOV) and truncated CT for a human head phantom," *Proc. SPIE* **5745**, 583–590 (2005).
15. S. Vijayan et al., "A real-time skin-dose mapping system for region-of-interest (ROI) fluoroscopy," *Med. Phys.* **42**, 3717–3717 (2015).
16. S. Vijayan et al., "Skin dose mapping for non-uniform x-ray fields using a backscatter point spread function," *Proc. SPIE* **10132**, 101320U (2017).
17. J. Zoetelief et al., "Patient dosimetry for x-rays used in medical imaging," *J. ICRU* **5**, 100 (2005).
18. I. Kawrakow and D. Rogers, "The EGSnrc system, a status report," in *Advanced Monte Carlo for Radiation Physics, Particle Transport Simulation and Applications*, NRCC Report PIRS-701 (2006).
19. B. Walters, I. Kawrakow, and D. W. O. Rogers, *DOSXYZnrc User's Manual*, NRCC Report PIRS-794 (2005).
20. G. Poludniowski et al., "SpekCalc: a program to calculate photon spectra from tungsten anode x-ray tubes," *Phys. Med. Biol.* **54**(19), N433–N438 (2009).
21. S. N. S. Vasan et al., "Design considerations for a dose-reducing region of interest (ROI) attenuator built in the collimator assembly of a fluoroscopic interventional C-arm," *Med. Phys.* **40**(6), 112 (2013).
22. I. G. Zubal et al., "Computerized three-dimensional segmented human anatomy," *Med. Phys.* **21**(2), 299–302 (1994).
23. D. R. Bednarek et al., "Verification of the performance accuracy of a real-time skin-dose tracking system for interventional fluoroscopic procedures," *Proc. SPIE* **7961**, 796127 (2011).
24. Z. Xiong et al., "A system for automatically calculating organ and effective dose for fluoroscopically-guided procedures," *Med. Phys.* **42**(6), 3583–3583 (2015).
25. Z. Xiong et al., "Automatic calculation of organ and effective dose for CBCT and interventional fluoroscopic procedures," *Med. Phys.* **43**(6), 3749–3749 (2016).
26. Z. Xiong et al., "Lens of the eye dose calculation for neuro-interventional procedures and CBCT scans of the head," *Proc. SPIE* **9783**, 97832V (2016).
27. G. X. Ding, D. M. Duggan, and C. W. Coffey, "Accurate patient dosimetry of kilovoltage cone-beam CT in radiation therapy," *Med. Phys.* **35**, 1135–1144 (2008).
28. J. Deng et al., "Kilovoltage imaging doses in the radiotherapy of pediatric cancer patients," *Int. J. Radiat. Oncol. Biol. Phys.* **82**, 1680–1688 (2012).
29. J. Zhao et al., "Investigation of dose for the triple-source computed tomography based on Monte Carlo simulations," *J. Imaging Sci.* **1**(1), 1–7 (2016).
30. F. A. Cucinotta et al., "Space radiation and cataracts in astronauts," *Radiat. Res.* **156**(5), 460–466 (2001).
31. B. V. Worgul et al., "Cataracts among Chernobyl clean-up workers: implications regarding permissible eye exposures," *Radiat. Res.* **167**(2), 233–243 (2007).
32. G. Chodick et al., "Risk of cataract after exposure to low doses of ionizing radiation: a 20-year prospective cohort study among US radiologic technologists," *Am. J. Epidemiol.* **168**(6), 620–631 (2008).
33. D. Teunen et al., "The European directive on health protection of individuals against the dangers of ionising radiation in relation to medical exposures (97/43/EURATOM)," *J. Radiol. Prot.* **18**, 133–137 (1998).
34. E. M. Weiss and O. Thabit, "Clinical considerations for allied professionals: radiation safety and protection in the electrophysiology lab," *Heart Rhythm* **4**, 1583–1587 (2007).
35. K. Perisinakis et al., "Accurate assessment of patient effective radiation dose and associated detriment risk from radiofrequency catheter ablation procedures," *Circulation* **104**, 58–62 (2001).
36. T. Moritake et al., "Dose measurement on both patients and operators during neurointerventional procedures using photoluminescence glass dosimeters," *Am. J. Neuroradiol.* **29**, 1910–1917 (2008).
37. M. Kezerashvili, S. Rudin, and D. R. Bednarek, "Automatic filter placement device for region of interest (ROI) fluoroscopy," *Health Phys.* **72**(1), 141–146 (1997).
38. P. Massoumzadeh, S. Rudin, and D. R. Bednarek, "Filter material selection for region of interest radiologic imaging," *Med. Phys.* **25**(2), 161–171 (1998).

**Zhenyu Xiong** is pursuing his doctoral degree in medical physics at the University at Buffalo (SUNY). As a graduate research assistant under Dr. Daniel R. Bednarek, he has worked to improve the dose tracking system (DTS). Areas of interest include Monte Carlo simulation on patient's organ and effective dose and determination of patient radiation dose during diagnostic imaging procedures.

**Sarath Vijayan** is a PhD student at the State University of New York at Buffalo. He has been engaged in the research and development of a real-time skin DTS software, Monte Carlo simulations on patient dose in imaging procedures, and evaluation of high-resolution x-ray imaging detectors.

**Stephen Rudin** is the director of the Radiation Physics Division, Department of Radiology, State University of New York at Buffalo, where he also serves as SUNY distinguished professor. He is the founding director of the Medical Physics Graduate Program at UB and a founding codirector of the UB-Toshiba Stroke and Vascular Research Center. He has been engaged in researching and developing high-resolution x-ray imaging detectors, dose reduction methods, and endovascular devices such as asymmetric stents. He has worked with major theoretical and clinical implications for medical physics, biomedical engineering, and diagnostic radiology.

**Daniel R. Bednarek** received his PhD in medical physics from the University of Chicago. He is a professor of radiology at the State University of New York at Buffalo and has been engaged in research in region-of-interest imaging including development and evaluation of limited-field-of-view, high-resolution real-time imaging detectors with specific application to neuroimaging. Recent work has focused on determination of patient radiation dose and development of a real-time DTS for interventional fluoroscopic procedures.